Available online at www.sciencedirect.com

jmr&t Journal of Materials Research and Technology

journal homepage: www.elsevier.com/locate/jmrt

Original Article

ZnAl hydrotalcites modified with nanocomposites nZVI–PAA for environmental remediation

Sorelis Nieto-Zambrano [a], Esthela Ramos-Ramírez [a,*], Francisco Tzompantzi Morales [b], Daria Camilla Boffito [c], Rafik Naccache [d], Norma L. Gutiérrez Ortega [e], Marta I. Litter [f], Sandra Cipagauta-Díaz [b], Aida Liliana Barbosa-López [g]

[a] Chemistry Department, Naturals and Exacts Science Division, Guanajuato Campus, University of Guanajuato, w/n Noria Alta, Guanajuato, GTO, C.P. 36050, México

[b] Department of Chemistry, Metropolitan Autonomous University-Iztapalapa, San Rafael Atlixco Av. No. 186, México, 09340, D.F., México

[c] Department of Chemical Engineering, Polytechnique de Montreal, C.P. 6079, Succ. CV, Montreal, H3C 3A7, QC, Canadá

[d] Department of Chemistry and Biochemistry, Concordia University, Montreal, H4B 1R6, QC, Canadá

[e] Department of Civil and Environmental Engineering, Engineering Division, Guanajuato Campus, University of Guanajuato, 77 Juárez St., Downtown, Guanajuato, GTO, C.P. 36000, México

[f] IIIA – Instituto de Investigación e Ingeniería Ambiental, CONICET, Universidad de San Martín, Campus Miguelete, Av. 25 de Mayo y Francia, 1650, San Martín, Prov. de Buenos Aires, Argentina

[g] Department of Chemistry, Exacts and Naturals Science Division/University of Cartagena, Zaragocilla Campus, Cartagena, Colombia

ARTICLE INFO

Article history:
Received 7 April 2021
Accepted 19 June 2021
Available online 20 July 2021

Keywords:
Pre-agglomeration reduction method
Nano-zero valent iron (nZVI)
Immobilizer
nZVI–PAA hybrid
Fe–PAA–ZnAl hybrid nanocomposite

ABSTRACT

Diffraction patterns of polyacrylic acid (PAA) encapsulated-(Fe)-modified ZnAl hydrotalcite (ZnAlH) showed the integration of Fe in the H lattice, resulting in a hybrid nanocomposite (Fe-PAA-ZnAlH), which was mainly verified with the characteristic shift in the 59–63° (2θ) region of the ZnAlH (110) reflection plane. The rise in the unit cell parameters (c and **a**) as the Fe % incremented, denoted incorporation of Fe in the ZnAlH red. Nonetheless, changes in the immobilizer molecular weight (PAA MW) from 1250 kDa to 5.1 kDa did not cause a difference in the distance between layers (c parameter) but in the cation-cation separation (**a** parameter), which meant that the nanoparticle was not located between layers, but in the lattice. The resulting band gap energies of the calcined hybrid nanocomposites were among 1.07–1.21 eV, which is an additional support of Fe^{+3} integration, suggesting insertion of Fe^{+3} 3d orbitals between the valence and the conduction band of ZnO. Furthermore, nZVI were prepared through a pre-agglomeration reduction method, where COOH-groups were bound to metal cations. Initially, aqueous Fe^{+2} was bound to PAA [Fe^{+2}-PAA], then reduced to obtain enclosed hybrid (nZVI-PAA). Less stability and more aggregation were observed with the lower molecular weight PAA. Additionally, PAA dissociation caused by pH changes affected the clustering of the nZVI particles. At higher MW, the hydrodynamic

* Corresponding author.
E-mail address: ramosre@ugto.mx (E. Ramos-Ramírez).
https://doi.org/10.1016/j.jmrt.2021.06.055

diameter and size distribution become smaller and tighter, respectively, allowing a more monodispersed population with sphere shape and organized in core–shell beads chains.

1. Introduction

Zero-valent iron (ZVI) is one of the most applicable nanomaterials in biomedicine and wastewaters treatments. Since the mid-seventies, regular size ZVI has been used in contaminant removal [1–3]. However, recently nanosized nZVI has been the focus of interest as a booster in environmental remediation due to their strong reducing power. The metallic iron core acts as an electron source and the oxide shell (Fe_xO_y) facilitates the sorption of contaminants while ensuring electron transfer from the metal core to the target contaminant, thus, intervening in the reaction mechanism [3–5]. The particle size is inversely related to the reactivity, mobility in the medium and the electron–hole redox potential to achieve selective photochemical reactions due to quantum size effect and large surface area-to-volume ratio, which increase the density of the sites for adsorption and catalysis [6]. Hence, it is important to obtain nanoparticles under 100 nm with narrow size distribution and high surface area to assure an effective product in photocatalytic elimination of target refractory contaminants. Control of particle size and stability without compromising the main objective, such as contaminant removal, drug delivery, photocatalysis, magnetic resonance imaging (MRI), is crucial to attain the previous characteristics [1,7–13]. Therefore, strategies to control the size will favor more effective applications of nZVI [14–17].

Amongst other factors, a difficult aspect of nanoparticle synthesis is particle aggregation, which can be reduced through surface modification of the nZVI with dispersants, surfactants including polymers [1,8,9,18,19]. Polyelectrolytes type-polymers, such as polyacrylic acid (PAA), impart negative surface charge on the nZVI and provide an electrostatic double layer and electro-steric repulsion [1,9,13,20–23]. The polyacrylic acid (PAA), has desirable properties for photocatalysis in aqueous environment, such as hydrophilicity, transparency, resistance, photochemical and mechanical stability [24–28]. Besides, polyelectrolytes as PAA are very sensitive to pH. At low pH, the structure of its chain does not charge. Though, at higher pH, they are fully charged or dissociated [21,23,29–32]. Additionally, the final properties of the resulted composites depend not only on the chemical structure and ratio of the components but also on the physical configuration of the stabilizer, which is affected by its molecular weight, size, shape and dispersion degree of the formed particle in the medium that will also alter their practical use [7,15,21,33–35]. Kaczmarek et al. [28], reported the effects of the stabilizer type on the physicochemical properties of polyacrylic acid/Ag nanocomposite. However, they did not analyze the influence of the molecular weight (MW) of PAA. Recently, Sánchez et al. [36] investigated the effects of changing the molecular weight of the PAA on the size of magnetic iron oxide particles. They found that, as the MW rises, the particle size diminishes, and their distribution becomes narrower. Song et al. [15] performed different hydrothermal synthesis (180 °C) of iron oxide (magnetite, Fe_3O_4) with PAA of 3 different MW and studied the size distribution by dynamic light scattering (DLS). They observed the tendency of decreasing particle size and crystallinity when the MW of the dispersant rises. This was attributed to spatial arrangement of the PAA chains around the particle that could favor or inhibit the crystal growth.

Moreover, hydrotalcites (H), layered double hydroxides (LDH) or anionic clays are layered compounds consisting of brucite like-layers, where some M^{+2} are replaced by M^{+3}, thus, a positive charge is generated and compensated with anions and water molecules. Its general formula is $[M^{+2}_{1-x}\ M^{+3}_{x}\ (OH)_2]^{+x}\ A^{n-}_{x/n}\ yH_2O$, where M^{+2} and M^{+3} are divalent and trivalent cations, respectively. A^{-n} is the interlaminar anion and x is the molar ratio $M^{+3}/M^{+3} + M^{+2}$ between 0.2 and 0.4. Due to non-compensated charges and ion exchanger properties, diversity of chemical species (polyoxometalates, decavanadates $(V_{10}O_{28})^{6-}$, heptamolybdates $(Mo_7O_{24})^{6-}$, NO_3^-, OH^-, CO_3^{-2}, adipate, terephthalate, triethylenglycolate) have been used to modify H, such as MgAlH, ZnAlH, NiAlH, forming products with meaningful applications [37–40]. Furthermore, comparing protective and/or templating agents, inorganic chemically inert clays (like H) are more cost-effective, environmentally friendly and sustainable.

With the purpose of optimizing materials properties, different species have been introduced in ZnAlH, such as Au nanoparticles [41,42] and Cu_2O [43]. Zhang et al. [41] found that Au nanoparticles elevated the catalytic and adsorption performance, when testing it with methyl orange (MO) and obtained a saturated capacity of 627.51 mg/g. Mikami et al. [42] irradiated Au/Zn_2AlH (prepared via H reconstruction) by UV–Vis light and totally photo-decomposed 50 mg/L of phenol in 160 min. Wu. et al. [43] evaluated Cu_2O–ZnAlH in the visible-light-driven photodegradation of MO with a high photocatalytic activity (90.18%) and the removal (80%) was still significant after 3 cycles. Hadnadjev-Kostic et al. [44] tested TiO_2–ZnAlH in the degradation of methyl blue with better results than for TiO_2 alone, which confirmed the promotion of synergetic effects and complex interactions between the TiO_2 (3% mass) and ZnAl mixed oxides. None of the consulted literature, has introduced nZVI in specifically ZnAlH, as it was done in this work. To better disseminate the nanoparticles, reduce their aggregation and/or boost up their properties and stability, the integration of polymeric nanocrystalline particles in inorganic hybrids have been used to achieve functional nanocomposites [45–48]. Hybrid nanocomposites are a multiphase solid material where one of the phases has at least one dimension lower than 100 nm [49]. They are relatively new, contain single or multi-components (like 2 or 3-component H)

and additional materials that add other functionalities to the system [50,51]. Also, ZnAlH can play as a templating agent that will allow a convenient positional arrangement of the nanoparticles. In addition, the variety of H composition, their semiconducting properties and high adsorption capacity enables to tune the electronic density at the interface between the nanoparticles and H [42]. Furthermore, hydrotalcites are economic, facile to prepare in the laboratory and by memory effects recover its original structure, making even easier material reusing. Moreover, having hybrid properties, the herein proposed material will smoothly be recovered from environmental bodies using magnetic properties.

In this work, we report on the integration of synthesized nZVI–PAA with ZnAlH and how the MW of the polymeric immobilizer (PAA), used during synthesis to cover the nZVI, influences their characteristics such as size distribution of the obtained products. nZVI size and stability control as well as adequate positional arrangement of the immobilizer are desirable for large scale synthesis and field applications of these materials in water remediation. Additionally, the fact of combining nZVI–PAA with ZnAlH can bring out an interesting synergy that will favor future uses in water remediation, using them as adsorbents for heavy metals such as Cr, As, Cd, Pb, U, among others [52–54]. They could also be used in photocatalytic processes for the degradation of organic compounds such as pesticides, dyes, and drugs.

2. Methods

2.1. Chemicals and materials

The following reactives were used as received: $Zn(NO_3)_2.6H_2O$ (Sigma-Aldrich, CAS No. 10196-18-6), $Al(NO_3)_3.9H_2O$ (Sigma-Aldrich, CAS No. 7784-27-2), $(NH_2)_2CO$ (Sigma-Aldrich, CAS No. 57-13-6), $(C_3H_4O_2)_n$ (Aldrich MW 5.1 kDa, CAS No. 9003-04-7 and 1250 kDa CAS No. 9003-01-4), $FeSO_4 \cdot 7H_2O$ (Fisher, CAS No. 7782-63-0), $NaBH_4$, (Aldrich, CAS No. 16940-66-2), high purity Ar and N_2 gas (Praxair), C_2H_5OH, CH_3OK (Sigma Aldrich, CAS No. 865-33-8), mili-Q deionized H_2O. The materials used were heating plate, magnetic stirrers, centrifuge, flat bottom flask, pH meter, beakers of different capacities, graduated cylinders, muffle furnace, laboratory rack, desiccator, balance.

2.2. Synthesis methodology

2.2.1. Synthesis of ZnAl hydrotalcite

ZnAlH was prepared by the Urea method [55,56]. 3.528 mol of solid urea was added to the mixture of 0.1678 mol of $Al(NO_3)_3 \cdot 9H_2O$ and 0.5034 mol of $Zn(NO_3)_2 \cdot 6H_2O$ to obtain a Zn^{+2}/Al^{+3} and $(NH_2)_2CO/(Al^{+3} + Zn^{+2})$ molar fraction of 3.00. The whole solution was maintained at 70 °C for 36 h with constant stirring. The product was separated from the mother solution and washed with de-ionized water up to pH 7 of the washing waters. The solid was dried at 80 °C overnight and stored in a vial for further characterization.

2.2.2. Synthesis of nZVI–PAA

The reduction method with pre-agglomeration or post-binding approach was used with PAA as stabilizer and dispersant [13,22]. Water and all the solutions were previously purged with Ar gas for 10 min. First, 0.0716 mol of $FeSO_4 \cdot 7H_2O$ was weighted considering the stoichiometry of the following reaction and 0.0716 mol Fe^{+2}/1 mol BH_4^- was equal to 2.00:

$$2PAA{-}Fe^{+2} + BH_4^- + 3H_2O \rightarrow 2PAA{-}Fe^0 + BO_3^- + 5H_2 \quad (1)$$

After preparing 1L of 2% PAA solution, 100 mL PAA solution was placed in a 500 mL rounded flask at 150 rpm and left there for 1 h under vacuum. Subsequently, Ar bubbling was introduced periodically and according to the vacuum conditions. Then, the sonicated $FeSO_4$ solution was dropped slowly into the PAA solution while the vacuum was suspended, and the Ar bubbling continued. On this way, an initial encapsulation by PAA of the Fe^{+2} occurred. Even though, the addition of $FeSO_4$ finished, periodic Ar bubbling (on/off) continued according to vacuum conditions for 10 min more, and then, the addition of the reduction agent was started dropwise. Immediately after the $NaBH_4$ addition, a black precipitate corresponding to nZVI was observed. Later, the vacuum restarted and was maintained for 0.5 h, while the Ar flow was very much diminished, until H_2 bubbling was finished. The solid was centrifuged at 8000 rpm for 15 min and washed 5 times with 99% ethanol (anhydrous). The drying was performed in a vacuum oven at 40 °C overnight. The nomenclature is referred to as nZVI, meaning nano-zero valent iron nanoparticles, followed by the stabilizer MW (kDa), the initials of PAA and the letters b or a, for exposed to ambient air immediately after synthesis (8 h, not washing) and not exposed, respectively.

2.2.3. Synthesis of nZVI–PAA–ZnAlH

We adopted a blending approach as strategy [57] to prepare the hybrid nanocomposite of nZVI–PAA–ZnAlH. A determined amount of Fe^0 particles (identified as nZVI–1250PAA and nZVI–5.1PAA) corresponding to 1% and 5% with respect to the whole amount of ZnAlH, was dispersed in 100 mL of anhydrous C_2H_5OH at 700 rpm, while vacuum and N_2 bubbling was happening on-off, for 30 min. 1 mL of H_2O was added it and stirred for additional 15 min. Simultaneous but separately, 3.0013 g of ZnAlH was added to a 100 mL anhydrous C_2H_5OH at 1150 rpm and keep it for 30 min under on-off vacuum-N_2 gas bubbling. Later, the suspension of ZnAlH was poured into the Fe^0 nanoparticles alcoholic suspension, then, 10 mL of CH_3OK was added to it and kept the same stirring rate of 1150 rpm with on-off vacuum-N_2 gas bubbling for additional 30 min. As a proposed general synthesis mechanism, first, a hydrolysis occurs followed by a condensation and finally the incorporation of the Fe element in the hydrotalcite's red. Initially, the small added amount of H_2O acts as sparkling plug that moves the equilibrium towards oxidation of Fe^0. At the beginning, the addition of CH_3OK, as strong base completes the oxidation of Fe^0, then, intermediaries methoxy ($-FeOCH_3$) e hydroxy ($-FeOH$) could have been formed. Together with PAA, the polymerization of the previous units happens, facilitating the alteration of the crystalline red [58]. The synthesis finished with vacuum for 3 h more, then, centrifugation, filtration, and washing several times with anhydrous C_2H_5OH up to a pH around 8. Then, let it dry between 18 a 22 °C under a desiccator to characterize them.

2.3. *Characterizations and measurements*

X-ray diffractograms (XRD) were measured using a Brucker D2 Phaser Diffractometer with Cu Kα radiation (λ = 0.15405 nm), operated with 30 kV and 10 mA under continuous Positive Sensitive Detector (PSD) fast mode, over a range of 2θ between 10 and 70° with step size of 0.3° and 2 s counting time. The hydrodynamic diameter measurements (HD) were carried out using a Malvern Panalytical Zetasizer Nano-ZS (663 nm He–Ne laser with an angle of 90°) through Dynamic Light Scattering (DLS) analysis; the samples were sonicated for 30 min prior to DLS, 0.7 mL of solution and sample's concentration of 0.05 mg/L were used. Transmission electron microscopy (TEM) micrographs of the nZVI–1250PAA and nZVI–5.1PAA were taken with an Oxford TEM microscope operated at 200 kV and using a 4 megapixels Gatan ultrascan camera to acquire the images. Selected area electron diffractions (SAED) were acquired in specific zones to measure the interplanar distances of some crystals and energy dispersive X-ray spectroscopy (EDS) attached to the Oxford microscope was used to verify elements presence in the same areas. The ultraviolet–visible (UV–Vis) absorption spectra were performed on a Thermoscientific Evolution 220 UV–Vis spectrophotometer from 200 to 800 nm with integration sphere for diffuse reflectance. The instrument was set to a 2 nm bandwidth, scan speed of 420 nm/min and the data was processed using Thermo Insight software. The evaluation of the band gap energy (Eg) for the calcined samples was calculated using the Kubelka–Munk function:

$$F(R) = (1 - R)^2/2R \quad (2)$$

where R is the reflectance (%) from the converted UV absorption spectra.

3. Results and discussion

The XRD pattern of Fig. 1 agrees with the JCPDS ICDD 038-0486 [59,60] and showed the main reflection planes of ZnAl hydrotalcite or layered double hydroxide (LDH) as (003), (006), (102), (105), (110) and (113) corresponding to the peaks 11.6351; 23.4466; 34.6109; 39.2222; 60.3373 and 61.4699° (2θ) for a 3R polytype. The crystallite diameter calculated by means of the Debye–Scherrer equation [$\Gamma = K\lambda/\beta \cos\theta$] was 39.8563 nm and the calculated lattice parameters were c = 22.8200 Å and **a** = 3.0100 Å, respectively. c is related to the separation between the layers and **a** to the cation–cation distance in the octahedra of the brucite like layer [61].

Fig. 2 shows the thermal behavior in air of ZnAlH, which can be summarized in 3 temperature ranges of mass % loss with stabilization and structure collapsing starting around 400 °C. The first loss was between 24.65 and 147.62 °C corresponded to 3.2% mass loss; the next one was between 147.62 and 317.08 °C with 23.21% of the total mass; third loss between 317.08 and 657.40 °C with 4.46% mass loss. The first weight loss was ascribed to water weakly adsorbed on the surface (physisorbed H_2O) or water evaporation. The following bigger mass loss step indicated that more than one phenomenon was occurring, and it was attributed to dehydration, partial decarbonation and dehydroxilation. The dehydration can count for 2 processes assigned to loss of H_2O bonded to surface OH^- and interlaminar H_2O of greater strength [62–65].

Fig. 3 shows the XRD patterns of the enclosed nZVI. Two syntheses were divided in a and b. b was exposed to ambient air for 8 h and a was not. It is indicated that for nZVI–1250PAA, the iron was mainly in its Fe^0 state, characterized by the basic reflection at ~45.00° (2θ). This peak represents the Fe^0 body centered cubic (bcc) lattice plane (110) reflection. This predominant presence of slightly crystalline zero valent iron (Fe^0) agrees with the JCPDS ICDD 006-0696. Even though, nZVI–1250PAA, nZVI–1250PAAa and nZVI–5.1PAAa had an intense XRD peak of zero valent iron, they showed an oxyhydroxide low intensity peak at 27.50° (2θ, γ-FeOOH) coinciding with the JCPDS ICDD 008-0098. The diffractogram for nZVI–5.1PAA, synthesized with PAA of low molecular weight (LMW), showed the characteristic peak of FeOOH (27.50°) at significant intensity, meanwhile, nZVI–1250PAA synthesized with PAA of high molecular weight (HMW = 1250 kDa) had that same peak, yet its intensity ratio was lower and about 1:5 compared to its main peak at 45.00°. In the absence of PAA

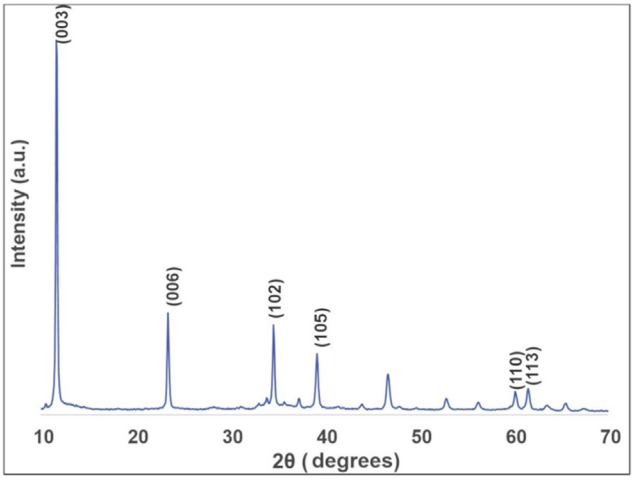

Fig. 1 – XRD diffractogram of ZnAl hydrotalcite.

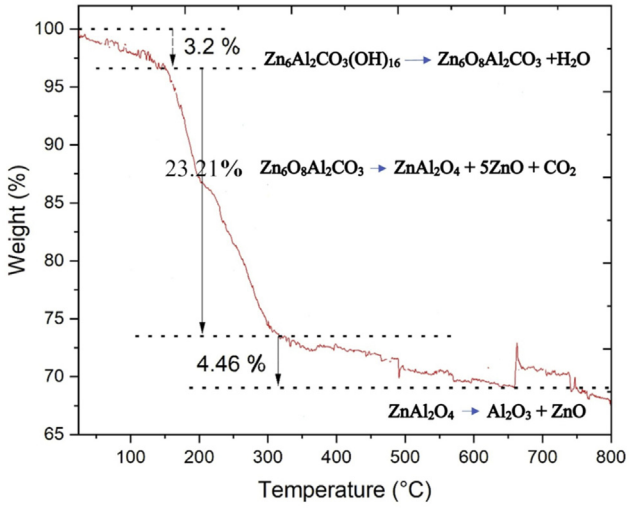

Fig. 2 – Thermogravimetric curve (TGA) for ZnAlH.

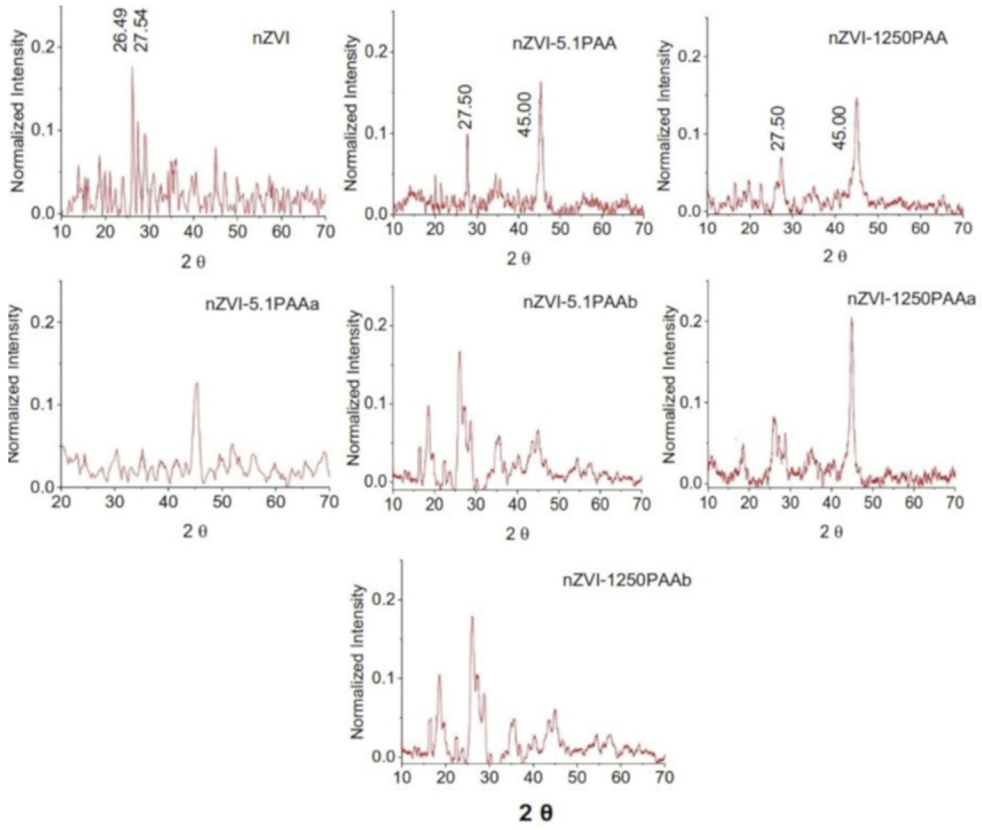

Fig. 3 – X-Ray Diffraction Pattern of the obtained nZVI.

(nZVI), the main peak for Fe^0 was observed but the presence of the most important peaks for the γ- and β-oxyhydroxide phases such as 27.54° (lepidocrocite, JCPDS-ICDD 05-0499) and 26.49° (akageneite, JCPDS-ICDD 42-1315), respectively, were highly noticeable [66–68]. Obviously, PAA MW had an effect, changing crystallinity and purity of the products. Also, the lack of PAA as in nZVI alone favored the formation of an incipient mixture of akaganeite and lepidocrocite. Furthermore, It is not only chelation and enclosure of the Fe when PAA is present, but also the fact that PAA acts as a barrier for humidity and oxygen [26,30,35,69]. Changes in the pH, as soon as the addition of $NaBH_4$ starts, favors the aperture of the PAA cover, that initially enclosed Fe^{+2}. While the pH is stabilized and the Fe^{+2} is reduced, a retro-enclosure with PAA occurs and results in Fe^0 recaptured by PAA [21,29]. Thus, the XRD of the products (Fig. 3) displayed the characteristic peak at 45.00 (2θ) for zero-valent iron and the TEM images (Fig. 6), clearly exhibit the PAA cover and the black center that mainly corresponded to Fe^0. Moreover, if a very low oxygen atmosphere and Ar bubbling are maintained simultaneously, oxidation will be avoided and a better control of the Fe^0 particle size is feasible. Likewise, the product synthesized with PAA MW of 5.1 kDa, with not exposure to air, also showed a well-defined peak for the α-Fe^0 (45.00°). If the fresh products are compared, the one synthesized with the higher MW, were less oxidized. For additional analysis, the products nZVI, nZVI–5.1PAA, nZVI–1250PAAa were chosen.

Being the mean hydrodynamic diameter (HD) depending upon the fluid properties and the surface of the particle, is a crucial measurement in this study. Dynamic light scattering (DLS) results was used to determine the mean HD and size distribution (Fig. 4 and Table 1). First, for nZVI–1250PAA in C_2H_5OH and H_2O (Fig. 4c and d), the HD diameter measurements showed less polydispersity, while the one synthesized without PAA (nZVI, Fig. 4a and b) was significantly polydispersed with a wide size range from 0 to 800 nm, in H_2O (Fig. 4b). These differences in polydispersity are explained by the PAA encapsulation and changes in pH introduced by the same solvent, knowing that the PAA pKa is equal to 4.8. Thus, at pH greater than 4.8, PAA will be highly dissociated and vice-verse. Hence, pH changes produce different charge density and conjugation of the PAA surface [28,30].

According to Song et al. [15], the tendency of particle size decreasing when PAA MW raises is related to the arrangement of the pH-responsive PAA chains around the particle. A straighter position of LMW PAA chains occurs while the HMW PAA chains lean to curl and enclose its chain around the particle surface, leading to a matrix constrain that avoid aqueous interactions. Obviously, the former behavior defines more individual particles, which are related to less clustered and more uniformly spread particles [70,71]. Secondly, a better stability and monodispersity are reached in C_2H_5OH and in the presence of PAA; the polydispersity and aggregation in aqueous media increased in PAA absence. For instance, 3 average groups of nZVI particles sizes, in H_2O, can be observed in the DLS graph (Fig. 4b). Upon comparison with that covered with PAA of LMW (nZVI–5.1PAA, Fig. 4f), the polydispersity index (PDI) of nZVI–$5.1PAA_{H_2O}$ was equal to 1.00, which is

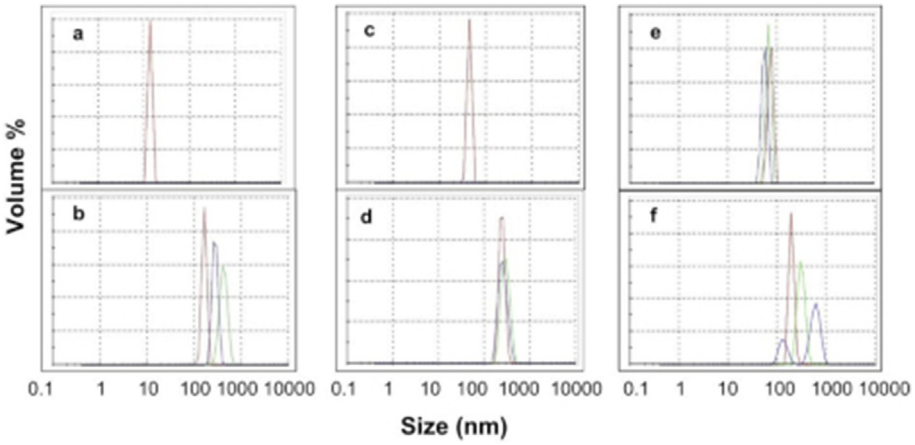

Fig. 4 – Size Distribution per volume % by DLS in CH_3CH_2OH and H_2O. a) nZVI-1 b) nZVI-2 c) nZVI–1250PAA-1 d) nZVI–1250PAA-2 e) nZVI–5.1PAA-1 f) nZVI–5.1PAA-2 1: CH_3CH_2OH; 2: H_2O.

greater than 0.700 and indicated that the sample had a very broad size distribution in H_2O as it is seen in Fig. 4f. Moreover, a more uniformed coverage of the nZVI is achieved with a HMW stabilizing agent. Furthermore, nZVI and nZVI–1250PAA behaved well in ethanol (Fig 4a, c), though nZVI–5.1PAA modestly did (Fig. 4e). nZVI and nZVI–1250 PAA had HD centered in approximately 40 nm. Aside from this, nZVI–1250PAA DLS graph presented 3 averaged sizes ranges in aqueous media (Fig. 4d), though such ranges were very closed. They were overlapped with an average centered HD radius of approximately 250 nm. Then, nZVI–1250PAA showed the most fairly behavior in H_2O (Fig. 4d), with a PDI of 0.687, which is within the acceptable PDI range (Table 1). It is desirable and convenient in water remediation, a mono-dispersed behavior and small mean particle size distribution such as in Fig. 4c. It can be inferred that pH ~7.0 (for instance, in C_2H_5OH with the lowest polydispersity index values) favors an appropriate binding between the COO– and the nano-zero valent iron particles. It is suggested that if the pH of the nZVI-1250PAA solutions is enlarged up to 7.0 and/or an adequate mixture of C_2H_5OH and H_2O is used, a substantial stabilization and mono-dispersity will be obtained. Therefore, more stabilization and homogeneous covering of the nZVI is achieved with greater MW. On the contrary, less stabilization and more polydispersity of particles synthesized with LMW PAA were observed.

Moreover, it is well known that nZVI had a core–shell structure where the outer layer is composed of iron oxide Fe_xO_y and its thickness can vary depending on the oxidation degree. The XRD of nZVI–PAA produced in this work evidenced a small percentage of iron oxyhydroxide (α-FeOOH) mainly, which most probably proceeded from the mentioned shell and can be converted to Fe_2O_3 or other oxide. On the other hand, the functional group of the used stabilizing agent (PAA (carboxylate, COO–)) will be the one bound to the nanoparticle. First of all, this binding interaction will be with $Fe^{+2/+3}$ (Lewis acid) from the metal oxide found on the outer layer of the Fe^0 core, and it is well stable because of the high affinity of the COO– for metals [16]. Sánchez et al. [36] mentioned that it could be several interactions possibilities between the PAA and oxidized iron. In this work, that oxidized iron come from the shell surface, and it is the one that directly bound to the COO– of the PAA because the interactions with the Fe^0 (core) will fall short and depend on the thickness of the nanoparticle shell and hence, on the degree of oxidation. Those interactions are affected by medium pH and could be unidentate, bidentate and bridging (Fig. 5).

Likewise, Huang et al. [13] presented their approach consisting in the construction of a polyelectrolyte multilayer where the polyelectrolyte (PAA) usually acts as a nanoreactor where the carboxylic acid group is the one able of binding ferrous/ferric cations in aqueous solution. Furthermore, Tombácz et al. [72] agreed with an H-bonding mechanism as in structure IV (Fig. 5) between the COO– and iron at pH of 6.5 corresponding to a PAA dissociation degree of 0.6. 6.5 was the approximated pH of the nZVI–PAA aqueous solution of the present report. Additionally, He et al. [16] agreed that COO– groups are expected to play a profound role in particle stabilization due to their stronger binding power with metals, which support a great stability of the obtained nanocomposite (nZVI–PAA). Because this pH (~6.5) of nZVI–PAA aqueous solution is higher than the pKa of 4.3, the COO– groups are almost fully dissociated and thus can interplay stronger with $Fe^{+2/+3}$ cations (Lewis acids). With the previous background, it is possible to predict that the objective material of this work, can perform well in environmental remediation. The modification of the iron nanoparticles with the stabilizing agent PAA will significatively benefit dye and heavy metal absorption due to the presence of the COOH group [57], exchange and

Table 1 – Polydispersity index of the samples.

Sample name	Polydispersity index ± std
$nZVI_{CH3CH2OH}$	0.543 ± 0.1
$nZVI_{H2O}$	1.000 ± 0.0
$nZVI–1250PAA_{CH3CH2OH}$	0.331 ± 0.0
$nZVI–1250PAA_{H2O}$	0.687 ± 0.1
$nZVI–5.1PAA_{CH3CH2OH}$	0.399 ± 0.1
$nZVI-5.1PAA_{H2O}$	1.000 ± 0.1

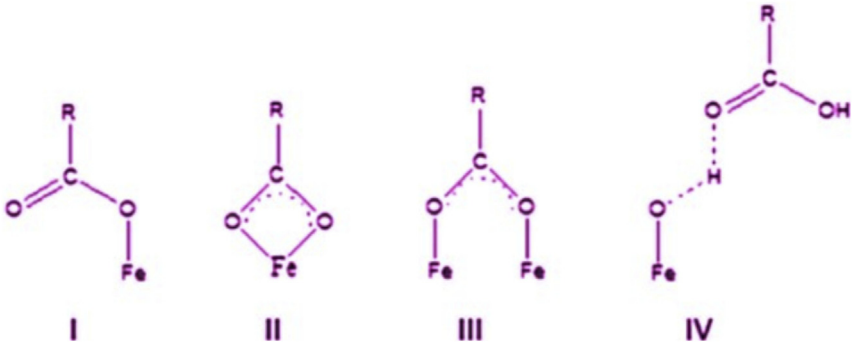

Fig. 5 – Possible interactions between the PAA and Fe present in Fe_xO_y [36].

oxide–reduction properties plus magnetic and electrostatic attractions. The different interactions will be the keys that will play significantly in the hypothesized catalytic and absorption capacity. The incorporation of iron and polyacrylic acid into the ZnAl hydrotalcite will favor the future accomplishments of this hybrid nanocomposite because of the stability, selectivity, catalytic and absorption capacity that characterize these materials.

Differences in microstructure between the materials without the ZnAlH, were studied by TEM. nZVI–1250PAAa and nZVI–5.1PAA were selected because they revealed less impurity and better XRD characteristics, for further analysis. TEM analysis was used to determine crystal size, absolute diameter, interplanar distances and define morphology of the nanoparticles. Fig. 6A–H and I–6 show the microscopy results of nZVI–1250PAAa and nZVI–5.1PAA, respectively. Fig. 6A–C exhibit defined cumulus of material that falls in the nanosized range (40–60 nm) and a chain of beads and branches arrangement. Same observation was noted for nZVI–5.1PAA (Fig. 6I, J, M, N). In Fig. 6D is shown the Selected Area Electron Diffraction (SAED, from white circle (eds 1) in Fig. 6A), that pointed out 3 interplanar distances equivalents to 2.04, 1.44 and 1.18 Å for nZVI–1250PAAa. If Fig. 6B is augmented, different directions of the crystallographic planes are distinguished with blue arrows in Fig. 6E, indicating a polycrystalline material. Thus, Fig. 6F shows a single crystal with planes in one direction and the crystal size can be estimated between 40 and 50 nm, coinciding with HD diameter of around 40 nm determined by DLS. Also, the TEM images 6B, 6E and 6K are evidence of a core–shell structure and the EDS spectrum from eds 1 (Fig. 6G, nZVI–1250PAAa and Fig. 6O, nZVI–5.1PAA) supports the fact that the marked circled area as eds 1, described as the core, was mostly composed of Fe^0. Additionally, nZVI–1250PAAa EDS spectrum (eds 2, 6H from Fig. 6A) indicated that there was a comparable amount of O and Fe, suggesting that the marked circled area as eds 2, was mostly composed of an iron oxide and coinciding with the shell. Also, the O can be partially attributed to PAA ($(C_3H_4O_2)_n$). This same observation is discerned in Fig. 6P (for nZVI–5.1PAA) and an evidence that PAA was present and encapsulating the nZVI. Moreover, starting with letter I, Fig. 6I–P shows the TEM images for nZVI–5.1PAA. The SAED for nZVI–5.1PAAa (Fig. 6L), indicated the interplanar distances of the main XRD reflection planes equals to 2.05, 1.46 and 1.19 Å. Also, it was distinguished a chainlike and branches structure for nZVI–5.1PAAa. It was seen a better defined and extended beads-and-branches morphology for nZVI–1250PAAa and more uniformed and compacted core–shell structure when it was compared to nZVI–5.1PAAa. In Fig. 6P (eds 2, outer area of Fig. 6J), the ratio of Fe:O peak's intensity for nZVI–5.1PAAa, was like the one in Fig. 6O, indicating an extended oxidation in nZVI–5.1PAAa. It is possible to estimate that the size varies from 40 to 100 nm for the product synthesized with PAA 5.1 kDa. Two different peaks in the EDS for Fe corresponded to 2 electronic transitions of Fe for the line Kα (6.398 KeV) and Lα (0.700 KeV), respectively. The peak at 0 KeV is due to noise of the internal electronic parts of the equipment. All the micrographs (except the SAED and EDS) displayed particles capped with the PAA net. Particles were less uniformed with PAA 5.1 kDa and the size of those cumulus of material fell in a wider range of sizes.

The X ray patterns of the modified ZnAlH hydrotalcites with selected nZVI–1250PAAa and nZVI–5.1PAA are presented in Fig. 7. In the non-calcined hybrid nanocomposites, the XRD pattern indicated that the hydrotalcite phase structure is maintained (JCPDS ICDD 038-0486), notwithstanding, small differences were observed in a zoom of discrete 2θ ranges (59–63° and 29–32.50° (2θ)). Additionally, the intensity of the hydrotalcite diffraction pattern main peak (11.658°, 2θ), highly related to its crystallinity, in the original ZnAlH is lower than for Fe–PAA–ZnAlH, which can be explained with the solvothermal like preparation that started with mixture of ZnAlH and nZVI–PAA in alcoholic suspension to obtain the Fe–PAA–ZnAlH. This process benefited a recrystallization of the hydrotalcite structure and resulted in an increased crystallinity of the final Fe–PAA–ZnAlH product. That means that the nZVI–PAA could have been a center for ZnAl LDH recrystallization and growth, and it could be a way to control the synthesis, also [57].

Furthermore, the mentioned intensity was less for 5% than for 1% of nZVI–PAA (Table 2). The inverse proportion between the intensity and the percentage of nZVI–PAA within the Fe–PAA–ZnAlH were explained by the presence of PAA in the hybrid compound because as a polymer, PAA tends to be amorphous and displays less crystallinity. Big difference in intensity was not seen, when the MW was changed and the nZVI–PAA was kept the same.

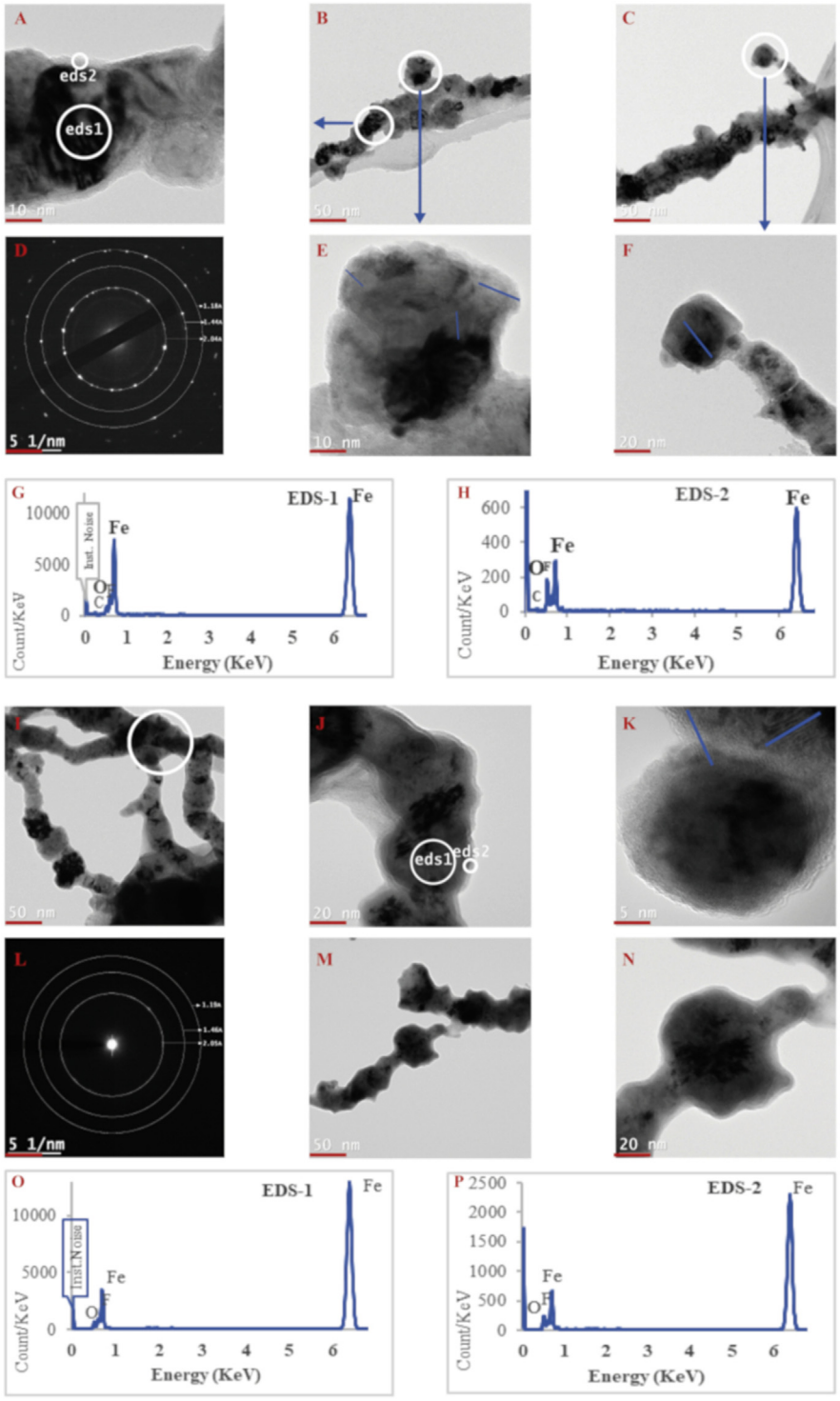

Fig. 6 – Electron microscopy and spectroscopy characterization of nZVI–1250PAAa and nZVI–5.1PAA. A) A view of TEM image for nZVI–1250PAAa (10 nm). B) TEM image for nZVI–1250PAAa (50 nm). C) TEM image for nZVI–1250PAAa (50 nm). D) SAED of A. E) Enlargement of white circle from B. F) Enlargement of white circle from C, G) EDS of white circle, eds 1 from A. H) EDS of white circle, eds 2 from A. I) A view of TEM image for nZVI–5.1PAA (50 nm). J) TEM image of nZVI–5.1PAA (20 nm resolution). K) TEM images of the nZVI–5.1PAA (5 nm resolution). L) SAED of I. M) TEM image of nZVI–5.1PAA (50 nm resolution). N) Enlargement from M. O) EDS of white circle 1 in J (eds 1). P) EDS of the white circle 2 in J (eds 2).

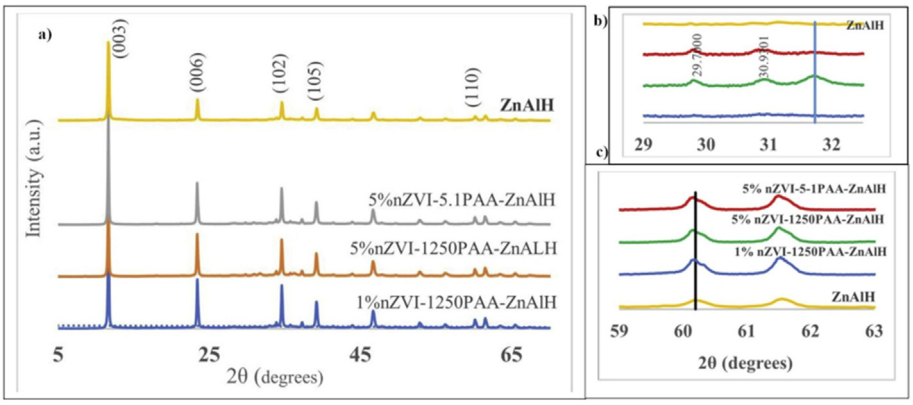

Fig. 7 – a) Diffractograms of the non-calcined hybrid nanocomposites – percentage weights 1% and 5% of nZVI–PAA particles in the hybrid nanocomposites w/ZnAlH. b) Enlargement of the 29–32.5° (2θ) region. c) Enlargement of the (110) reflection plane zone 59–63° (2θ).

Small differences were detected in the XRD pattern of hybrid nanocomposites in the region 29.00–32.50° (2θ, Fig. 7b). Peaks such as 29.70, 30.93°(2θ) were observed in the 5% Fe–1250PAA–ZnAlH and 5% Fe–5.1PAA–ZnAlH and obviously, they are not discerned in the original XRD pattern of ZnAlH.

Furthermore, for both annealed samples at 400 °C (c-5% Fe–1250PAA–ZnAlH and c-5% Fe–5.1PAA–ZnAlH, Fig. 8a), the diffractograms displayed mostly ZnO or zincite and Fe_2O_3 or hematite (JCPDS ICDD 036-1451 and 039-1346, respectively). The peak width of the ZnO was large, which signaled a ZnO small size crystal (nanosized range). The only difference between c-5% Fe–1250PAA–ZnAlH and c-5% Fe–5.1PAA–ZnAlH was the greater intensity of the 34.50° (2θ) peak in c-5% Fe–1250PAA–ZnAlH (Fig. 8b) attributed to hematite [73]. Obviously, at 400 °C calcination temperature, there is not traces of the PAA, but the presence of different metal oxide phases has remained. It was inferred that the synthetic procedure to get the hybrid composite Fe–PAA–ZnAlH with HMW PAA, endowed the calcination product with better crystallinity.

Fig. 7c shows a zoom of the 59–63° (2θ) region, where the reflection corresponding to the crystallographic plane (110) can be seen. A slight shift of the (110) reflection peak towards lower 2θ, can be observed in the samples containing nZVI–PAA and it moved to the left as nZVI–PAA percentage become greater (for instance, ZnAlH $2\theta_{(110)} = 60.21°$ to 5% Fe–1250PAA–ZnAlH $2\theta_{(110)} = 60.11°$). This shift for the (110) peak allows to suggest incorporation of Al^{+3} by Fe^{+3} (Al^{+3} and Fe^{+3} ionic radius are 0.53 Å and 0.65 Å, respectively) in the hydrotalcite lattice [63,73,74]. This difference in ionic radius suggests perturbations in the crystalline lattice, which causes small stress in it and displacement of that signal towards lower 2θ. Furthermore, the inclusion of Fe^{+3} into the lattice was verified by the proportional increment in a unit cell parameter and since the Fe^{+3} has a larger ionic radius than Al^{+3}, complies with Vegard's law, also. Hence, nZVI brought a slight raise in a parameter which was directly proportional to the percentage of iron with the same PAA MW. The trend in crystal size was greater for higher proportion of nZVI–PAA with the same PAA MW and diminished when this proportion was constant and the PAA MW dropped off. Also, the remarkable difference of PAA MW (1250 kDa–5.1 kDa) at the same % of nZVI–PAA, influenced the hybrid nanocomposites crystal size (53.7597–51.3667 nm). A significant difference was remarked when the obtained ZnAlH crystal size (39.8563 nm) was compared with the one of the hybrid nanocomposites at any of the percentage used (51.3703, 53.7597 and 51.3667 nm for 1% Fe–1250PAA–ZnAlH, 5% Fe–1250PAA–ZnAlH and 5% Fe–5.1PAA–ZnAlH, respectively). Obviously, the whole crystal size gets bigger with the introduction of nZVI–PAA which conforms with the increment in crystalline cell parameters. This crystal size should not be related to the hydrodynamic diameter or particle size because these parameters are affected by environmental conditions, however, the crystal size is not.

More on that, the upsurge of the basal parameters when the nanocomposite particle percentage raises, confirmed incorporation of the Fe-PAA in the ZnAlH. a parameter gets bigger when the proportion of nZVI–PAA enlarged (3.0100 Å for ZnAlH to 3.0712 Å in 5% Fe–1250PAA–ZnAlH) and slightly diminished from 5% Fe–1250PAA–ZnAlH to 5% Fe–5.1PAA–ZnAlH (3.0712 Å–3.0693 Å), when there was a change in PAA MW from 1250 kDa to 5.1 kDa. In consequence, modification of the MW from 1250 kDa to 5.1 kDa did not cause

Table 2 – Lattice parameters of the % x Fe–PAA–ZnAlH.

Name	d (Å)	I (count/s)	c parameter	a parameter	Crystal size (nm)
ZnAlH	7.5991	22,902	22.8200	3.0100	39.8563
1% Fe–1250PAA–ZnAlH	7.5715	44,368	22.7145	3.0684	51.3703
5% Fe–1250PAA–ZnAlH	7.5841	33,854	22.7523	3.0712	53.7597
5% Fe–5.1PAA–ZnAlH	7.5841	33,998	22.7523	3.0693	51.3667

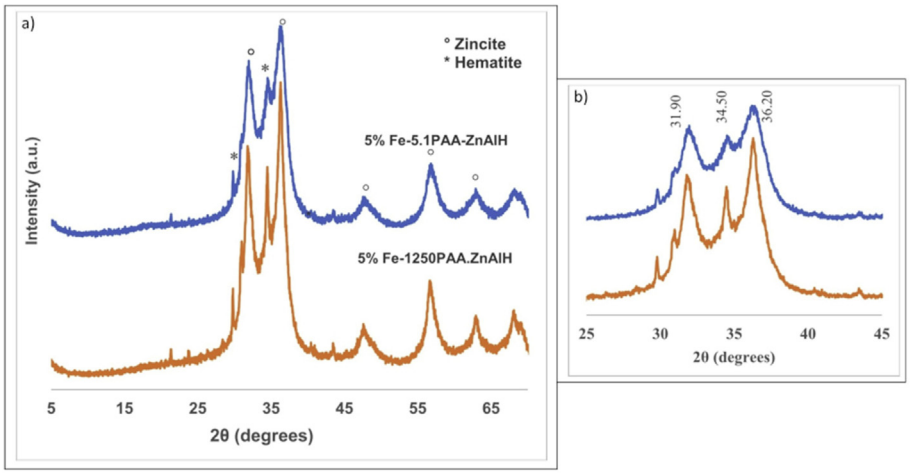

Fig. 8 – a) Diffractograms of the calcined hybrid nanocomposites – percentage weight 5%. b) Enlargement view of the XRD zone 25–45 (2θ) of the calcined hybrid composites. Compounds calcined at 400 °C, according to the thermal analysis of the ZnAlH.

a difference in the distance between layers but in the cation–cation separation on the octahedra of the layer. The bigger the PAA MW that encloses the nanoparticles, the bigger is the cation–cation distance (within the brucite like-layer), forcing the cations to separate more and allow access. When the MW was kept constant and % of nZVI increased, there was an increment in all the parameters.

The Eg for calcined Fe-PAA nanocomposites and hybrid nanocomposites (Fe–PAA–ZnAlH) were less than for calcined ZnAlH and within the visible region. Additionally, the annealed sample with any of the percentage used of nanoparticles nZVI–PAA, showed a shift to lower Eg with respect to calcined cZnAlH. Mantilla's group [73], obtained a ternary hydrotalcite of ZnAlFe by coprecipitation. They started with the mixture of the 3 metallic nitrates ($Zn(NO_3)_2$, $Al(NO_3)$, $Fe(NO_3)_3$) under high basic conditions. After calcination, Mantilla's group obtained the mixed oxides with Eg between 2.54 and 2.04 eV. In this present work, a solid solution of metallic oxides with Eg among 1.07–1.21 eV (Table 3) has been obtained, which make them more suitable for solar photodegradation. It is known that ZnO and Fe_2O_3 have a Eg of 3.2 eV and 2.2 eV, respectively. In this work, the Eg for all the metallic mixtures or composites, has fallen in the visible region except for cZnAlH. The UV–Vis absorption capacity of the cZnAlH changed when it was altered with the nZVI–PAA nanocomposite. cZnAlH initial absorption was centered in approximately 350 nm and had a hypsochromic shift to 285 nm (c1% Fe–1250PAA–ZnAlH), 283.90 nm (c5% Fe–1250PAA–ZnAlH) and 284.60 nm (c5% Fe–5.1PAA–ZnAlH). Those shifts can be explained with the insertion of the 3d orbitals of Fe^{+3} between the valence and conduction band of mostly ZnO material resulting from the samples annealing [75]. In the calcined hybrid nanocomposites, the Fe^{+3} can act as trap site for photogenerated electrons to easy the photocarriers separation. The trapped electrons can react with the electron acceptors and reduce O_2 to $^{-}O_2$. Meanwhile, Fe^{+3} can intervene in the valence holes and oxidize OH^- or H_2O molecules to •OH species [75]. The formula of indirect band gap energy was applied for the hybrid nanocomposite because it was found to be more adequate in this case.

Table 3 – Band gap energy of the samples.

Sample nomenclature	Eg (eV)
c-ZnAlH	3.10 eV
c-nZVI1250	1.78 ev
c-nZVI5.1	1.71 eV
c5% Fe-5.1PAA-ZnAlH	Indirect Eg = 1.21 eV
c5% Fe-1250PAA-ZnAlH	Indirect Eg = 1.21 eV
c1% Fe-1250PAA-ZnAlH	Indirect Eg = 1.07 eV

Recent studies regarding this type of material have described their utility as adsorbents. Bian et al. [76], used nZVI modified with anionic and cationic polymers for the removal of Cr (VI) and proposed a combined mechanism of oxidation/reduction of Cr (VI)/Cr (III), coprecipitation and adsorption. They confirmed the oxide-reductive potential of nZVI in adsorption systems [76]. Yu et al. [77] used LDH supported nZVI for the adsorption of U (VI). They found sites on LDH–nZVI that favored a greater uptake of U (VI) in aqueous solutions, which was attributed to adsorption and reduction actives points [77]. In addition, Zhou et al. [78] used Fe–MgAl–LDH magnetic nanoparticles to adsorb organic compounds and established an analytical method for the extraction and quantification of organic pollutants such as phenol and its derivatives with such a composite [78]. Besides, Kong et al. [53] synthesized nZVI dispersed on LDH composite to remove V (V) from simulated groundwater, following DFT calculations. The adsorbed V (V) was reduced to V (IV) and V(III) by nZVI and spontaneously transformed into VO_2 and V_2O_3. This work showed the potential of the composite to serve as an efficient material for the immobilization of V(V) in groundwater.

Based on the above and given the good semiconductor properties identified in the synthesized hybrid nanocomposites Fe–PAA–ZnAlH obtained in this research, its high potential to be used in processes of catalytic photodegradation of persistent organic compounds is considered, such as for

pesticides, dyes, drugs, among other molecules; This application has not been studied with this hybrid nanocomposites, however, there are numerous degradation studies with LDH in different metallic combinations and molar ratios using metals such as Mg, Al, Fe, Co, Cu, Zn among others [78–80]. Obtaining Fe–PAA–ZnAlH with low Eg and memory effect to be used in elimination of persistent organic pollutants, broaden the options for a great diversity of studies in future environmental remediation research.

4. Conclusions

Herein, it has been integrated nZVI–PAA with ZnAlH. The diffractograms patterns of the non-calcined products indicated Fe introduction in the hydrotalcite crystalline red and with the calcination, the hydrotalcite structure was destroyed and a metallic oxides solid solution of ZnO with small amount of Fe_2O_3 was formed. This provided a new route to obtain such a metal oxide mixture. Hence, the calcination of these nanocomposites generated a similar result as if the preparation started with ternary ZnAlFe hydrotalcites. The resulting semiconducting properties are interesting and forecast a successful application in the visible photocatalysis for environmental remediation. Their band gap energies were lower than for the two traditionally benchmark photocatalysts, ZnO and TiO_2. Moreover, the best behavior in H_2O of the nZVI–PAA was observed for nZVI–1250PAA, synthesized with HMW PAA. Furthermore, the stabilizing agent offered an additional humidity and oxygen barrier that contributed to the anoxic conditions and therefore, to the purity of the products. At higher molecular weights, the hydrodynamic diameter and size distribution become smaller and tighter, respectively, allowing a more monodispersed population. It is introduced a different way to obtain this oxide solid solution. This synthesized nZVI–PAA nanocomposite with a size range of 40–60 nm (with HMW PAA) may found application in biomedicine as well as in water/soil remediation. This report predicts this material versatility with an application broad spectrum within the technical and scientific scope. In future contributions, this solid mixture will be tested in photodegradation of contaminated water and the results will be shared.

Declaration of Competing Interest

The authors declare that they have no known competing financial interests or personal relationships that could have appeared to influence the work reported in this paper.

Acknowledgments

Sincere thanks to CONACYT (México) and University of Guanajuato (Guanajuato, México) for their financial support. The authors are also grateful for the collaboration of Nanomaterials Laboratory (Concordia University, Montréal, QC, Canadá) and the Center for Characterization and Microscopy of Materials (CM)^2 (Polytechnique de Montréal, Montréal, QC, Canadá).

REFERENCES

[1] Fu F, Dionysiou DD, Liu H. The use of zero-valent iron for groundwater remediation and wastewater treatment: a review. J Hazard Mater 2014;267:194–205. https://doi.org/10.1016/j.jhazmat.2013.12.062.
[2] Cheong S, Ferguson P, Hermans IF, Jameson GNL, Prabakar S, Herman DAJ, et al. Synthesis and stability of highly crystalline and stable iron/iron oxide core/shell nanoparticles for biomedical applications. Chempluschem 2012;77:135–40. https://doi.org/10.1002/cplu.201100074.
[3] O'Carroll D, Sleep B, Krol M, Boparai H, Kocur C. Nanoscale zero valent iron and bimetallic particles for contaminated site remediation. Adv Water Resour 2013;51:104–22. https://doi.org/10.1016/j.advwatres.2012.02.005.
[4] Cook SM. Assessing the zero valent iron nanoparticles technology for remediation at contaminated sites. Office of solid Wastes and Emergency Response. Office of Superfund remediation and Technology Innovation. Washington, DC: US Environmental Protection Agency.; 2009. p. 1–9. https://clu-in.org/download/studentpapers/zero-valent-iron-cook.pdf.
[5] Freyria FS, Esposito S, Armandi M, Deorsola F, Garrone E, Bonelli B. Role of pH in the aqueous phase reactivity of zerovalent iron nanoparticles with acid orange 7, a model molecule of azo dyes. J Nanomater 2017;2017:1–13. https://doi.org/10.1155/2017/2749575.
[6] Petronella F, Truppi A, Ingrosso C, Placido T, Striccoli M, Curri ML, et al. Nanocomposite materials for photocatalytic degradation of pollutants. Catal Today 2017;281:85–100. https://doi.org/10.1016/j.cattod.2016.05.048.
[7] Cuenya BR. Synthesis and catalytic properties of metal nanoparticles: size, shape, support, composition, and oxidation state effects. Thin Solid Films 2010;518:3127–50. https://doi.org/10.1016/j.tsf.2010.01.018.
[8] Ambika S, Nambi IM, Senthilnathan J. Low temperature synthesis of highly stable and reusable CMC-Fe^{2+}(-nZVI) catalyst for the elimination of organic pollutants. Chem Eng J 2016;289:544–53. https://doi.org/10.1016/j.cej.2015.12.063.
[9] Chen X, Ji D, Wang X, Zang L. Review on nano zero valent iron (nZVI): from modification to environmental applications. IOP Conf Ser Earth Enviro Sci 2016;51:1–7. https://iopscience.iop.org/article/10.1088/1742-6596/51/1/012004.
[10] Li XQ, Elliott DW, Zhang WX. Zero-valent iron nanoparticles for abatement of environmental pollutants: materials and engineering aspects. Crit Rev Solid State Mater Sci 2006;31:111–22. https://doi.org/10.1080/10408430601057611.
[11] Kubacka A, Fernández-García M, Colón G. Advanced nanoarchitectures for solar photocatalytic applications. Chem Rev 2012;112:1555–614. https://doi.org/10.1021/cr100454n.
[12] Obare SO, Meyer GJ. Nanostructured materials for environmental remediation of organic contaminants in water. J Environ Sci Heal A Toxic Hazard Subst Environ Eng 2004;39:2549–82. https://doi.org/10.1081/LESA-200027010.
[13] Huang Q, Shi X, Pinto RA, Petersen EJ, Weber WJ. Tunable synthesis and immobilization of zero-valent iron nanoparticles for environmental applications. Environ Sci Technol 2008;42:8884–9. https://doi.org/10.1021/es8015588.
[14] Demortière A, Panissod P, Pichon BP, Pourroy G, Guillon D, Donnio B, et al. Size-dependent properties of magnetic iron oxide nanocrystals. Nanoscale 2011;3:225–32. https://doi.org/10.1039/c0nr00521e.

[15] Song Y, Li Y, Teng Z, Huang Y, Chen X, Wang Q. Size-Controlled synthesis of carboxyl-functionalized magnetite particles: effects of molecular weight of the polymer and aging. ACS Omega 2018;3:17904–13. https://doi.org/10.1021/acsomega.8b02351.
[16] He F, Zhao D. Manipulating the size and dispersibility of zerovalent iron nanoparticles by use of carboxymethyl cellulose stabilizers. Environ Sci Technol 2007;41:6216–21. https://doi.org/10.1021/es0705543.
[17] Gupta AK, Gupta M. Synthesis and surface engineering of iron oxide nanoparticles for biomedical applications. Biomaterials 2005;26:3995–4021. https://doi.org/10.1016/j.biomaterials.2004.10.012.
[18] Farrell D, Majetich SA, Wilcoxon JP. Preparation and characterization of monodisperse Fe nanoparticles. J Phys Chem B 2003;107:11022–30. https://doi.org/10.1021/jp0351831.
[19] Prasad Rao J, Gruenberg P, Geckeler KE. Magnetic zero-valent metal polymer nanoparticles: current trends, scope, and perspectives. Prog Polym Sci 2015;40:138–47. https://doi.org/10.1016/j.progpolymsci.2014.07.002.
[20] Burke NAD, Stover HDH, Dawson FP. Magnetic nanocomposites: preparation and characterization of polymer coated iron nanoparticles. Chem Mater 2002;14:4752–61. https://doi.org/10.1021/cm020126q.
[21] Guo Y, Van Ravensteijn Bas GP, Evers CHJ, Kegel WK. pH Reversible encapsulation of oppositely chatrged colloids mediated by polyelectroloites. Langmuir 2017;33:4551–8. https://doi.org/10.1021/acs.langmuir.7b00845.
[22] He F, Zhao D, Liu J, Roberts CB. Stabilization of Fe – Pd nanoparticles with sodium carboxymethyl cellulose for enhanced transport and dechlorination of trichloroethylene in soil and groundwater. Ind Eng Chem Res 2007;46:29–34. https://doi.org/10.1021/ie0610896.
[23] Ishiduki K, Esumi K. The effect of pH on adsorption of poly(acrylic acid) and poly(vinylpyrrolidone) on alumina from their binary mixtures. Langmuir 1997;13:1587–91. https://doi.org/10.1021/la960804l.
[24] Kataby G, Ulman A, Prozorov R, Gedanken A. Coating of amorphous iron nanoparticles by long-chain alcohols. Langmuir 1998;14:1512–5. https://doi.org/10.1021/la970978i.
[25] Laumann S, Micić V, Lowry GV, Hofmann T. Carbonate minerals in porous media decrease mobility of polyacrylic acid modified zero-valent iron nanoparticles used for groundwater remediation. Environ Pollut 2013;179:53–60. https://doi.org/10.1016/j.envpol.2013.04.004.
[26] Lim M, Kim D, Seo J. Enhanced oxygen-barrier and water-resistance properties of poly(vinyl alcohol) blended with poly(acrylic acid) for packaging applications. Polym Int 2016;65:400–6. https://doi.org/10.1002/pi.5068.
[27] Lin J, Wu J, Yang Z, Pu M. Synthesis and properties of poly(acrylic acid)/montmorillonite superabsorbent composites. Polym Polym Compos 2001;9:469–71. https://doi.org/10.1177/096739110100900704.
[28] Kaczmarek H, Metzler M, Węgrzynowska-Drzymalska K. Effect of stabilizer type on the physicochemical properties of poly(acrylic acid)/silver nanocomposites for biomedical applications. Polym Bull 2016;73:2927–45. https://doi.org/10.1007/s00289-016-1617-3.
[29] Wiśniewska M, Urban T, Grzadka E, Zarko VI, Gun'ko VM. Comparison of adsorption affinity of polyacrylic acid for surfaces of mixed silica-alumina. Colloid Polym Sci 2014;292:699–705. https://doi.org/10.1007/s00396-013-3103-x.
[30] Liufu S, Xiao H, Li Y. Adsorption of poly(acrylic acid) onto the surface of titanium dioxide and the colloidal stability of aqueous suspension. J Colloid Interface Sci 2005;281:155–63. https://doi.org/10.1016/j.jcis.2004.08.075.
[31] Dong H, He Q, Zeng G, Tang L, Zhang C, Xie Y, et al. Chromate removal by surface-modified nanoscale zero-valent iron: effect of different surface coatings and water chemistry. J Colloid Interface Sci 2016;471:7–13. https://doi.org/10.1016/j.jcis.2016.03.011.
[32] Chen SA, Lee HT. Structure and properties of poly(acrylic acid)-doped polyaniline. Macromolecules 1995;28:2858–66. https://doi.org/10.1021/ma00112a035.
[33] Gaumet M, Vargas A, Gurny R, Delie F. Nanoparticles for drug delivery: the need for precision in reporting particle size parameters. Eur J Pharm Biopharm 2008;69:1–9. https://doi.org/10.1016/j.ejpb.2007.08.001.
[34] Nyiro-Kosa I, Rečnik A, Pósfai M. Novel methods for the synthesis of magnetite nanoparticles with special morphologies and textured assemblages. J Nanoparticle Res 2012;14:1–13. https://doi.org/10.1007/s11051-012-1150-8.
[35] Tiraferri A, Chen KL, Sethi R, Elimelech M. Reduced aggregation and sedimentation of zero-valent iron nanoparticles in the presence of guar gum. J Colloid Interface Sci 2008;324:71–9. https://doi.org/10.1016/j.jcis.2008.04.064.
[36] Sanchez LM, Martin DA, Alvarez VA, Gonzalez JS. Polyacrylic acid-coated iron oxide magnetic nanoparticles: the polymer molecular weight influence. Colloids Surf A Physicochem Eng Asp 2018;543:28–37. https://doi.org/10.1016/j.colsurfa.2018.01.050.
[37] Bravo-Suárez JJ, Páez-Mozo EA, Oyama ST. Review of the synthesis of layered double hydroxides: a thermodynamic approach. Quim Nova Soc Bras Quim 2004;27:601–4. https://doi.org/10.1590/S0100-40422004000400015.
[38] Doeuff M, Kwon T, Pinnavaia TJ. Layered double hydroxides pillared by polyoxometalate anions: EXAFS studies and chemical synthesis. Synth Met 1989;34:609–15. https://doi.org/10.1016/0379-6779(89)90447-5.
[39] Dimotakis ED, Pinnavaia TJ. New route to layered double hydroxides intercalated by organic anions: precursors to polyoxometalate-pillared derivatives. Inorg Chem 1990;29:2393–4. https://doi.org/10.1021/ic00338a001.
[40] Veteška M, Pospíšil M, Melánová K, Beneš L, Zima V. Structure analysis of hydrotalcite intercalated with pyrenetetrasulfonate; experiments and molecular modelling. J Mol Model 2008;14:1119–29. https://doi.org/10.1007/s00894-008-0355-3.
[41] Zhang YX, Hao XD, Kuang M, Zhao H, Wen ZQ. Preparation, characterization and dye adsorption of Au nanoparticles/ZnAl layered double oxides nanocomposites. Appl Surf Sci 2013;283:505–12. https://doi.org/10.1016/j.apsusc.2013.06.136.
[42] Mikami G, Grosu F, Kawamura S, Yoshida Y, Carja G, Izumi Y. Harnessing self-supported Au nanoparticles on layered double hydroxides comprising Zn and Al for enhanced phenol decomposition under solar light. Appl Catal B Environ 2016;199:260–71. https://doi.org/10.1016/j.apcatb.2016.06.031.
[43] Wu X, Zhang D, Jiao F, Wang S. Visible-light-driven photodegradation of methyl orange using Cu_2O/ZnAl calcined layered double hydroxides as photocatalysts. Colloids Surf A Physicochem Eng Asp 2016;508:110–6. https://doi.org/10.1016/j.colsurfa.2016.08.047.
[44] Hadnadjev-Kostic M, Vulic T, Marinkovic-Neducin R, Lončarević D, Dostanić J, Markov S, et al. Photo-induced properties of photocatalysts: a study on the modified structural, optical and textural properties of TiO_2–ZnAl layered double hydroxide based materials. J Clean Prod 2017;164:1–18. https://doi.org/10.1016/j.jclepro.2017.06.091.
[45] Giuri A, Masi S, Colella S, Listorti A, Rizzo A, Liscio A, et al. GO/PEDOT:PSS nanocomposites: effect of different dispersing agents on rheological, thermal, wettability and

electrochemical properties. Nanotechnology 2017;28:174001. https://doi.org/10.1088/1361-6528/aa6517.
[46] Alayo N, Paniello A, Striccoli M, Lucia Curri M, Pérez-Murano F. Towards individual electrical contact of nanoparticles in nanocomposites. Microelectron Eng 2011;88:2439–43. https://doi.org/10.1016/j.mee.2011.02.059.
[47] Bonnefond A, Mičušík M, Paulis M, Leiza JR, Teixeira RFA, Bon SAF. Morphology and properties of waterborne adhesives made from hybrid polyacrylic/montmorillonite clay colloidal dispersions showing improved tack and shear resistance. Colloid Polym Sci 2013;291:167–80. https://doi.org/10.1007/s00396-012-2649-3.
[48] Bonnefond A, González E, Asua JM, Leiza JR, Kiwi J, Pulgarin C, et al. New evidence for hybrid acrylic/TiO_2 films inducing bacterial inactivation under low intensity simulated sunlight. Colloids Surf B Biointerfaces 2015;135:1–7. https://doi.org/10.1016/j.colsurfb.2015.07.034.
[49] Giannelis EP. Polymer layered silicate nanocomposites. Adv Mater 1996;8:29–35. https://doi.org/10.1002/adma.19960080104.
[50] Utracki LA, Kamal MR. Clay-containing polymeric nanocomposites. Arab J Sci Eng 2002;27:43–67. https://nrc-publications.canada.ca/eng/view/accepted/?id=8c1bcda1-b9b4-4019-9b40-799c4c39695e.
[51] Ludueña L, Morán J, Alvarez V. Biodegradable polymer/clay nanocomposites. In: Kumar-Thakur V, Kumari-Thakur M, editors. Eco-friendly polymer nanocomposites. 75th ed. Magdeburg, Germany: Springer US; 2015. p. 109–35. https://doi.org/10.1007/978-81-322-2470-9.
[52] Sheng G, Hu J, Li H, Li J, Huang Y. Chemosphere enhanced sequestration of Cr (VI) by nanoscale zero-valent iron supported on layered double hydroxide by batch and XAFS study. Chemosphere 2016;148:227–32. https://doi.org/10.1016/j.chemosphere.2016.01.035.
[53] Kong X, Chen J, Tang Y, Lv Y, Chen T, Wang H. Enhanced removal of vanadium (V) from groundwater by layered double hydroxide-supported nanoscale zerovalent iron. J Hazard Mater 2020;392:122392. https://doi.org/10.1016/j.jhazmat.2020.122392.
[54] Zhou Q, Lei M, Li J, Zhao K, Liu Y. Sensitive determination of bisphenol A , 4-nonylphenol and 4-octylphenol by magnetic solid phase extraction with Fe @ MgAl-LDH magnetic nanoparticles from environmental water samples. Sep Purif Technol 2017;182:78–86. https://doi.org/10.1016/j.seppur.2017.01.071.
[55] Tzompantzi F, Mantilla A, Bañuelos F, Fernández JL, Gómez R. Improved photocatalytic degradation of phenolic compounds with ZnAl mixed oxides obtained from LDH materials. Top Catal 2011;54:257–63. https://doi.org/10.1007/s11244-011-9656-3.
[56] Inayat A, Klumpp M, Schwieger W. The urea method for the direct synthesis of ZnAl layered double hydroxides with nitrate as the interlayer anion. Appl Clay Sci 2011;51:452–9. https://doi.org/10.1016/j.clay.2011.01.008.
[57] Liu X, Pang H, Liu X, Li Q, Zhang N, Mao L, et al. Orderly porous covalent organic frameworks-based materials: superior adsorbents for removal from aqueous solutions. Innovation 2021;2:100076. https://doi.org/10.1016/j.xinn.2021.100076.
[58] Ramos-Ramirez E. Obtencion de Hidrotalcitas por el Proceso Sol-Gel [Ph.D. dissertation]. Guanajuato, México: University of Guanajuato; 1997.
[59] Liu Q, Wang B, Wang C, Tian Z, Qu W, Ma H, et al. Basicities and transesterification activities of Zn-Al hydrotalcites-derived solid base. Green Chem 2014;16:2604–13. https://doi.org/10.1039/C3GC42648C.
[60] Wen Y, Zhao Y, Lu L, Zhang SJ, Xu B. Electrochemical performance of Zn-Al double layered hydroxide for supercapacitor application. IOP Conf Ser Mater Sci Eng 2017;250:1–7. https://doi.org/10.1088/1757-899X/250/1/012055.
[61] Ramos-Ramírez E, Gutiérrez-Ortega NL, Tzompantzi-Morales F, Del Ángel GA, Martínez-Gómez C, Pabón-Gelves E. Effect of the Mg/Al ratio on activated sol-gel hydrotalcites for photocatalytic degradation of 2,4,6-trichlorophenol. Int J Photoenergy 2017;2017:1–9. https://doi.org/10.1155/2017/5373482.
[62] Tzompantzi F, Mendoza-Damián G, Rico JL, Mantilla A. Enhanced photoactivity for the phenol mineralization on ZnAlLa mixed oxides prepared from calcined LDHs. Catal Today 2014;220–222:56–60. https://doi.org/10.1016/j.cattod.2013.07.014.
[63] Suárez-Quezada M, Romero-Ortiz G, Suárez V, Morales-Mendoza G, Lartundo-Rojas L, Navarro-Cerón E, et al. Photodegradation of phenol using reconstructed Ce doped Zn/Al layered double hydroxides as photocatalysts. Catal Today 2016;271:213–9. https://doi.org/10.1016/j.cattod.2016.01.009.
[64] Perioli L, Nocchetti M, Ambrogi V, Latterini L, Rossi C, Costantino U. Sunscreen immobilization on ZnAl-hydrotalcite for new cosmetic formulations. Microporous Mesoporous Mater 2008;107:180–9. https://doi.org/10.1016/j.micromeso.2007.02.021.
[65] Vágvölgyi V, Palmer SJ, Kristof J, Frost RL, Erzsébet H. Mechanism for hydrotalcites decomposition: a controlled rate thermal analysis study. J Colloid Interface Sci 2008;318:302–8. https://doi.org/10.1016/j.jcis.2007.10.033.
[66] Fu D, Keech PG, Sun X, Wren JC. Iron oxyhydroxide nanoparticles formed by forced hydrolysis: dependence of phase composition on solution concentration. Phys Chem Chem Phys 2011;13:18523–9. https://doi.org/10.1039/c1cp20188c.
[67] Encina ER, Distaso M, Klupp Taylor RN, Peukert W. Synthesis of goethite α-FeOOH particles by air oxidation of ferrous hydroxide Fe(OH)2 suspensions: insight on the formation mechanism. Cryst Growth Des 2015;15:194–203. https://doi.org/10.1021/cg501191h.
[68] Takahashi Y, Matsubara E, Suzuki S, Okamoto Y, Komatsu T, Konishi H, et al. In-situ X-ray diffraction of corrosion products formed on iron surfaces. Mater Trans 2005;46:637–42. https://doi.org/10.2320/matertrans.46.637.
[69] Lucas-Granados B, Sánchez-Tovar R, Fernández-Domene RM, García-Antón J. A pH study for the degradation of acetaminophen with iron oxide nanostructures. Chem Eng Trans 2019;73:139–44. https://doi.org/10.3303/CET1973024.
[70] Kendall K, Kendall M, Rehfeldt F. Adhesion of cells, viruses and nanoparticles. 1st ed. Netherlands: Springer; 2011. p. 169–93. https://doi.org/10.1007/978-90-481-2585-2.
[71] Folarin OM, Sadiku ER, Maity A. Polymer-noble metal nanocomposites: review. Int J Phys Sci 2011;6:4869–82. http://hdl.handle.net/10204/5625.
[72] Tombácz E, Szekeres M, Hajdú A, Tóth IY, Bauer RA, Nesztor D, et al. Colloidal stability of carboxylated iron oxide nanomagnets for biomedical use. Period Polytech Chem Eng 2014;58:3–10. https://doi.org/10.3311/PPch.7285.
[73] Mantilla A, Tzompantzi F, Fernández JL, Góngora JAID, Gómez R. Photodegradation of phenol and cresol in aqueous medium by using Zn/Al + Fe mixed oxides obtained from layered double hydroxides materials. Catal Today 2010;150:353–7. https://doi.org/10.1016/j.cattod.2009.11.006.
[74] Prince J, Tzompantzi F, Mendoza-Damián G, Hernández-Beltrán F, Valente JS. Photocatalytic degradation of phenol by semiconducting mixed oxides derived from Zn(Ga)Al layered double hydroxides. Appl Catal B Environ 2015;163:352–60. https://doi.org/10.1016/j.apcatb.2014.08.019.

[75] Liu X, Ma R, Zhuang L, Hu B, Chen J, Liu X, et al. Recent developments of doped g-C_3N_4 photocatalysts for the degradation of organic pollutants. Crit Rev Environ Sci Technol 2021;51:751–90. https://doi.org/10.1080/10643389.2020.1734433.

[76] Bian H, Wan J, Muhammad T, Wang G, Sang L, Jiang L, et al. Computational study and optimization experiment of nZVI modified by anionic and cationic polymer for Cr (VI) stabilization in soil: kinetics and response surface methodology (RSM). Environ Pollut 2021;276:116745. https://doi.org/10.1016/j.envpol.2021.116745.

[77] Yu S, Wang X, Liu Y, Chen Z, Wu Y, Liu Y, et al. Efficient removal of uranium (VI) by layered double hydroxides supported nanoscale zero-valent iron: a combined experimental and spectroscopic studies. Chem Eng J 2019;365:51–9. https://doi.org/10.1016/j.cej.2019.02.024.

[78] Zhou S, Li C, Zhao G, Liu L, Yu J, Jiang X, et al. Heterogeneous co-activation of peroxymonosulfate by CuCoFe calcined layered double hydroxides and ultraviolet irradiation for the efficient removal of p - nitrophenol. J Mater Sci Mater Electron 2019;30:19009–19. https://doi.org/10.1007/s10854-019-02258-0.

[79] Yang W, Zhou M, Oturan N, Bechelany M, Cretin M. Highly efficient and stable Fe II/Fe III LDH carbon felt cathode for removal of pharmaceutical ofloxacin at neutral pH. J Hazard Mater 2020;393:122513. https://doi.org/10.1016/j.jhazmat.2020.122513.

[80] Yang B, Liu J, Liu Z, Wang Y, Cai J, Peng L. Preparation of chitosan/Co-Fe-layered double hydroxides and its performance for removing 2, 4-dichlorophenol. Environ Sci Pollut Control Ser 2019;26:3814–22. https://doi.org/10.1007/s11356-018-3886-x.